PCCP

The Charge Reduction Rate for Multiply Charged Polymer Ions via Ion-Ion Recombination at Atmospheric Pressure

Journal:	*Physical Chemistry Chemical Physics*
Manuscript ID	CP-ART-07-2020-003989.R1
Article Type:	Paper
Date Submitted by the Author:	04-Oct-2020
Complete List of Authors:	Tamadate, Tomoya; Kanazawa University Higashi, Hidenori; Kanazawa University Hogan Jr., Christopher; University of Minnesota, Mechanical Engineering Seto, Takafumi; Kanazawa University

The Charge Reduction Rate for Multiply Charged Polymer Ions via Ion-Ion Recombination at Atmospheric Pressure

Tomoya Tamadate[1], Hidenori Higashi[1,2], Christopher J. Hogan Jr.[3*], & Takafumi Seto[1,2*]

[1]Faculty of Natural System, Graduate School of Natural Science and Technology, Kanazawa University, Kanazawa, Japan
[2]Faculty of Frontier Engineering, Institute of Science and Engineering, Kanazawa University, Kanazawa, Japan
[3]Department of Mechanical Engineering, University of Minnesota, Minneapolis, MN, USA

Submitted to:

Phys Chem Chem Phys

*To whom correspondence should be address: Takafumi Seto: seto@t.kanazawa-u.ac.jp, Christopher J. Hogan: hogan108@umn.edu

Abstract

The charge reduction of multiply charged macromolecular ions via recombination with small ions in the gas phase is commonly employed to modulate the charge on macromolecules prior to mass spectrometric and mobility analyses. We employ a recently developed continuum-Molecular Dynamics (MD) calculation approach to determine the recombination rate coefficient of multiply charged (1 to 7 excess positive charged) polyethylene glycol ions (mass of 4600 Da) with smaller singly charged anions, modeled as NO_2^- ions. The continuum-MD approach accounts explicitly for the influence of the background gas on the recombination process, accounts explicitly for ion translational, vibrational, and rotational motion, and enables recombination rate coefficient calculation in nitrogen near atmospheric pressure, wherein neither low pressure nor high pressure recombination theories are strictly applicable. Continuum-MD simulations yield recombination rate coefficients near 3.9×10^{-14} m^3 s^{-1} for singly charged ions, increasing to 3.0×10^{-11} m^3 s^{-1} for the +7 ion. Pre-existing collision rate coefficient expressions for rigid ions are found to be within a factor of 2-5 of calculations for all charge states, but their use requires knowledge of an appropriate collision distance, which is not well-defined for flexible polymer ions. Continuum-MD-inferred rate coefficients are incorporated into a model of charge reduction, and the charge state distribution versus anion concentration determined with it is compared to charge reduction measurements made via atmospheric pressure differential mobility analysis. Good agreement is observed between simulations and experiments; although results are extremely sensitive to the recombination rate coefficients, experimental results are bounded by models utilizing rates within a factor of 2 (0.5-2.0x) of the continuum-MD rates.

Introduction

The ability to reduce the charge state of electrospray-generated, multiply charged macromolecular ions,[1, 2] including polymers,[3, 4] proteins,[5-8] and other biological molecules,[9] is important for a number of analytical methods, as it can enable improved molecular mass identification and distribution analyses in mass spectrometry,[10-12] mitigate Coulombic stretching during ion mobility measurements,[13] and enable better separation of different charge states from one another in mobility measurements without mass analysis.[14] In general, the charge state distribution on macromolecular electrospray-generated ions can be shifted to smaller values through two different means. First, cationic (for positively charged) solutes can be added to the electrospray solution which are prone to the formation ions via ion evaporation;[15, 16] ion evaporation depletes droplets of charge, leaving less charge for the macromolecular ion after solvent evaporation completes.[17-20] Second, small ions of the opposite polarity can be mixed with the macromolecular ions of interest[1] subsequent to completion of the electrospray process. This latter method has several advantages. Charge reduction via recombination of oppositely charged ions after the electrospray process carries on to completion, which follows multiple Coulomb fission steps,[21] significantly reduces adduct formation associated with in-droplet charge reduction.[14] Gas-phase ion-ion recombination can additionally be applied to a wide variety of ions; the recombination process is typically transport limited[22, 23] and not restricted to particular analyte chemical structures.

The design of ion-ion recombination based charge reduction schemes would require *a priori* calculation techniques for the recombination rate between a macromolecular ion of charge state z and a singly charged, smaller ion. However, present models are not applicable for such calculations at atmospheric pressure, and experimental data directly addressing multiply charged ion-ion recombination rates are lacking. The ion-ion recombination rate has

been a problem of long standing interest in gas phase chemical physics, dating back to the work of Thomson[24] (developing a three-body collision model applicable at low-pressure), Langevin[25] (developing a model accurate at high pressure), and Natanson,[26] Brueckner,[27] and Bates & Flannery[28] (attempting to bridge the transition regime between the low pressure and high pressure limits). However, disagreement between these earlier approaches and measurements are commonplace;[29-31] even for nanometer scale ions at atmospheric pressure neither the low pressure nor high pressure models are applicable and bridging models have only been modestly successful. Furthermore, traditional recombination rate calculation approaches largely assume interacting point charges. Macromolecular ions have been shown in numerous studies to adopt charge-state dependent structures because of Coulombic stretching. In particular, Fernandez de la Mora,[32, 33] Larriba,[34-36] and colleagues have shown that unbranched polymer chains adopt nearly linear structures at high charge state (which the polymer wrapped around individual charges), and as charge state decreases, polymer ions contain a multiply charged, larger core with one or more chains extended from the core. Eventually, at low enough charge state, macromolecular ions adopt globular structures comprised only of the core. De Pauw and colleagues also found that branched polymer ions adopt similar, charged state-dependent conformations.[37] Such structural transitions must be taken into account in determining multiply charged ion recombination rates, as must structural transition during the recombination process itself, i.e. the influences of an incoming small ion of the opposite polarity on the macromolecular ion structure need to be considered.

Recently, we developed a hybrid continuum-Molecular Dynamics calculation approach to evaluation ion-ion recombination rates,[38] which is based upon the framework developed by Filippov[39] and is applicable the transition regime for collision rate calculations. In this approach, when ions are sufficiently far from one another, relative motion is described by diffusion (continuum) equations, while within a critical distance,[40] Molecular Dynamics

(MD) simulations are utilized to monitor the motion of both ions. Ions are placed in separate subdomains with a limited number of gas molecules which only interact with their assigned ion, while ions still interact with one another. This permits simulations which correctly account for ion-neutral collision influences on ion trajectories. In prior work the simulation approach was verified via comparison of resulting recombination rate coefficients in He to the measurements of Lee & Johnsen,[30] yielding excellent agreement with their measurements near atmospheric pressure without any fitting coefficients applied. In this study, we adapt this approach to determine the recombination rate coefficient of multiply charged polyethylene glycol ions with a nominal molecular mass of 4600 Da (PEG_{4600}) and charge states of z = 1 to 7, in N_2 with NO_2^-. Recombination rate coefficients are used to constructa charge reduction model which is compared to experimental measurements of PEG_{4600}^{z+} charge reduction in air at atmospheric pressure.

Numerical & Experimental Methods

Continuum-Molecular Dynamics Simulations

The presented analysis makes use of both numerical simulations and ion (electrical) mobility based measurements to quantify multiply charged PEG_{4600}^{z+} ion-singly charged ion recombination reactions. We elect to present numerical simulations first, as our ultimate goal is to evaluate the potential of hybrid continuum-MD methods in recombination rate coefficient calculation.

The recombination rate coefficient between $PEG_{4600}^{z+}$and NO_2^- is denoted as β_z, and the recombination rate is equal to the product of β_z and the NO_2^- ion concentration. Recombination rate coefficient calculation was performed using the framework depicted in Figure 1. We considered a multiply charged PEG_{4600}^{z+} ion in the center of a spherical domain (the limiting sphere) of radius (δ), while an NO_2^- ion arrives on the limiting sphere surface.

Outside of the limiting sphere, the transport rate of the NO_2^- to the sphere surface can be described by diffusion equations (continuum approximation), while inside the limiting sphere transport is examined via MD simulation. As shown originally by Filippov,[39] and rederived in our recent work,[38] balancing the flux from outside the limiting sphere to inside yields the equations:

$$\beta_z = \frac{4\pi(D_z + D_-)\delta\Psi_\delta}{(1-exp(-\Psi_\delta))}\left(1 + \left(\frac{\pi}{2}\right)^{1/2}\frac{(2-p_\delta)}{p_\delta}Kn_\delta\frac{\Psi_\delta}{(exp(\Psi_\delta)-1)}\right)^{-1} \quad (1a)$$

$$\Psi_\delta = \frac{ze^2}{4\pi\varepsilon_0 k_b T\delta} \quad (1b)$$

$$Kn_\delta = \left(\frac{m_{red}}{k_b T}\right)^{1/2}\frac{(D_{z+} + D_-)}{\delta} \quad (1c)$$

where Ψ_δ is the ratio of electrical to thermal energy at the limiting sphere radius, Kn_δ is diffusive Knudsen number[41] for the limiting sphere, D_z and D_- are the diffusion coefficients of the multiply charged positive ion and the singly charged negative ion, respectively, ε_0 is the permittivity of vacuum, k_b is Boltzmann constant, T is temperature of the system (300 K) and m_{red} is the reduced mass of PEG_{4600}^{z+} and NO_2^-. A diffusion coefficient of 0.1402 $cm^2\ s^{-1}$ was utilized in calculations for NO_2^- while for PEG_{4600}^{z+} we used D_z = 7.24 x 10^{-3} $cm^2\ s^{-1}$, based on measurement of the electrical mobility for singly charged ions (described and reported subsequently) and application of the Stokes-Millikan equation.[42] While the diffusion coefficient is presumably lower for more highly charged, stretched ions, because $D_{z+} << D_-$, charge state-dependent diffusion coefficients do not strongly influence calculation results.

In equations (1a-c) all terms can be directly input except for δ, which must be chosen properly to ensure results are insensitive to this input, and p_δ, the probability that an NO_2^- ion entering the limiting sphere collides with the PEG_{4600}^{z+} ion. p_δ needs to be determined through the MD simulations. With regards to the former, the limiting sphere radius

specifically needs to be selected such that the choice of a larger radius would lead to an identical recombination rate coefficient. Optimization of δ is hence only necessary to maximize calculation efficiency; extremely large values (e.g. micrometer distances) provide accurate results, but such long ion travel distances drastically increase computational expense. In traditional calculations, δ is chosen using the approach of Fuchs,[40] based on derivations provided by Wright.[43] However, δ selected in this manner is not verified previously, requires an estimate of the physical sizes of the colliding species, and does not consider that the proper choice of δ may also depend upon long range interactions between colliding species. Therefore in this study, we empirically tuned δ in the manner described in the supporting information, and identify a δ_{crit} value beyond which the resulting recombination rate coefficients were insensitive to the choice of δ for each charge state. We examined δ values in the 355-3552 Å range, finding that $\delta_{\text{crit}} = 1761$ Å can be utilized for $z = 2 - 7$ and $\delta_{\text{crit}} = 1056.6$ Å can be applied for $z = 1$. Figure S1 of the supporting information displays plots of the recombination rate coefficient determined as a function of δ for the $z = 7$ and $z = 1$ charge states. As elaborated on in the conclusions section, while the continuum-MD approach is applicable to a broad range of ion-ion recombination reactions, in each implementation it is presently necessary to determine an appropriate value of δ such that the result is not sensitive to it, akin to time step sensitivity tests required in MD simulations.

p_δ was determined via molecular dynamics calculations as follows. Using a custom routine code adapted from the algorithms of LAMMPS,[44] we first made models of PEG_{4600}^{z+} and NO_2^- ions. For PEG_{4600}^{z+}, 105 ethylene glycol monomers (-CH2-CH2-O-, M_w= 44 Da) were arranged linearly and z NH_4^+ ions were placed on the molecule as adduct ions. NVT simulations (with temperature control via the velocity scaling method) were then performed with the general AMBER force field (GAFF)[45] with a time step of 0.01 fs for 10^7 steps (100

ps). Table S1 of the supporting information lists the partial charges on atoms within PEG ions while for NH_4^+ the partial charges were utilized from NIH (National Institute of Health) database values. After this first equilibration calculation, a larger time step of 0.5 fs was then utilized for 10^7 steps (5 ns) for further equilibration. This approach resulted in "equilibrated" PEG_{4600}^{z+} structures, as described in our previous work.[46] These operations were also performed on NO_2^-, again using partial charges from the NIH database. The final two structures were used as initial structures of the collision MD simulation. The thermally relaxed ions were placed in the simulation domain with a prescribed value for δ. The PEG_{4600}^{z+} ion, at the center of the domain, was rotated randomly prior to placement and had zero center-of-mass velocity. The NO_2^- ion, placed on the surface of the limiting sphere, was also rotated randomly and had an initial center-of-mass velocity (with angle of entry θ and speed v_0) sampled following the approach we describe previously,[38] which accounts for both Coulomb potential interaction with the central PEG_{4600}^{z+} ion and thermal influences. Sampled velocity vectors which would result in the NO_2^- ion leaving the domain were discarded and resampled. Around each ion, we placed 10^4 monoatomic nitrogen molecules, whose velocities were sampled from a Maxwell-Boltzmann distribution at 300 K. We used "monoatomic" nitrogen molecules to improve calculation speed; in preliminary calculations we found the inclusion of diatomic N_2 and gas rotational and vibrational energy did not strongly influence results as we could recover (within 2%) experimentally measured values of NO_2^- ion diffusion coefficients at 300 K via velocity auto-correlation function calculations with monoatomic N_2. To mimic atmospheric pressure conditions, the nitrogen molecules were placed within a cubic box of side length 745 Å. Gas molecules only interact with atoms within the ion of their assigned domain throughout the simulation; the Lennard-Jones potential parameters of monoatomic nitrogen were $\varepsilon = 0.144$ kcal mol^{-1} and $\sigma = 3.798$ Å (fit to the viscosity of N_2), and for interactions with atoms within ions we utilized the Lorentz–

Berthelot combining rules. In addition to Lennard-Jones terms, nitrogen molecules interacted with ions via an ion-induced dipole potential with a nitrogen polarizability of 1.7 $Å^3$. A description of how the ion-induced dipole potential was implemented is provided in the supporting information.

After initialization, velocity-Verlet based NVE simulations were carried out with a time step of 0.5 fs, hence ion translational, vibrational, and rotational degrees of freedom were accounted for in calculations. After each time step, each of the cubic domains was shifted such that their assigned ion's center-of-mass remained at the domain center. Because gas molecules only interact with their assigned ion, even when the domains overlap, the gas density around each ion remains constant. Periodic boundary conditions were invoked, such that gas molecules found outside their domain after each time step were reintroduced on the opposing side. Because ion-ion recombination leads to decreasing potential energy between ions as they approach one another, there is an increase in total system thermal energy, and the use of NVE simulations does lead to gas molecule heating as simulations proceed. However, because the number of gas molecules in each domain is significantly larger than the number of atoms in ions, this level of heating negligibly affects results. Each simulation resulted in either the two ions colliding or the ion-ion center-of-mass distance exceeding δ. Collision was considered to occur when the interatomic distance of any two atoms in the different ions was less than 5 Å; smaller distances were found to have a negligibly small influence on results. As expanded on in the *Results & Discussion* section, this distance is not related to a critical distance for actual charge transfer, but is instead related to the escape probability of ions from one another. Videos depicting simulations are provided in the supporting information, showing both the ions on close approach, and the motion of the two separate ion-containing domains about one another. Further details on such simulations are provided in our prior study.[38] For each charge state examined, simulations were repeated until 10^2

collision events were observed. p_δ was evaluated as the ratio of the number of collisions to total number of simulations. Subsequently, the values of δ and p_δ were input into equations (1a-c) to determine β_z. Poisson statistics yield an uncertainty in the determined rate of ±10%.

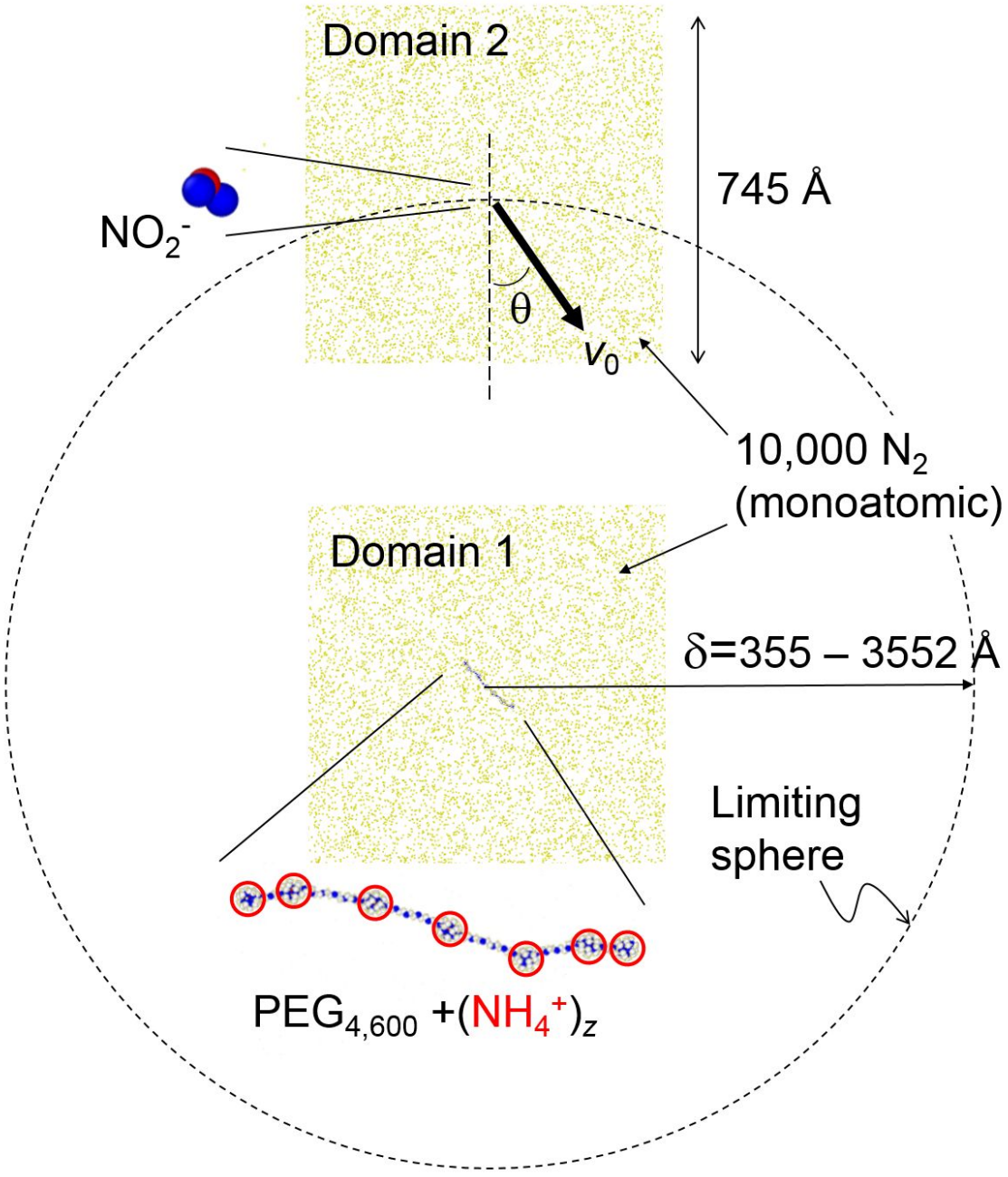

Figure 1. A schematic diagram of the molecular dynamics simulation setup used in recombination rate coefficient determination. θ and v_0 refer to the initial speed and entry angle for the NO_2^- into the limiting sphere.

Electrical Mobility Based Charge Reduction Measurements

The experimental setups depicted in figures 2(a) and (b) were utilized to examine the initial charge state distribution of PEG_{4600}^{z+} and ion-ion recombination-driven charge reduction, respectively. In both instances, an 1:1 methanol: water (MtOH:H_20) solution with PEG_{4600} (Wako Chemicals) at a concentration of 448 μM was electrosprayed using a tapered metal capillary (I.D. 110 mm and O.D. 240 mm) with constant flow rate of 1.67 μL min^{-1}, driven by a syringe pump. Ammonium acetate (NH_4Ac) at a concentration of 11 mM was utilized to provide sufficient electrical conductivity for the solution to be stably electrosprayed[6] with a DC voltage of ~2.5 kV applied to the capillary. Droplets were electrosprayed into ultra-high purity (UHP) air, which carried the generated ions at a constant flow rate of 3.0 L min^{-1} at room temperature and atmospheric pressure. Subsequently PEG_{4600}^{z+} ions were sampled in parallel by a Shimadzu LCMS-2020 single quadrupole mass spectrometer, yielding the mass-to-ratio (m/z) distribution for the ions up to 2000 Th, and an ion mobility spectrometer, yielding the ion/electrical mobility (Z_p) distribution. The ion mobility spectrometer was a differential mobility analyzer[47] (DMA, Wycoff, 1.8 cm classification length, inner radius of 2.5 cm, outer radius of 3.3 cm) operated with an inlet flow rate of 3.0 L min^{-1} and a recirculating filtered sheath flow rate of 128 L min^{-1}. DMAs act as mobility filters whose transmitted mobility is known from the instrument operating conditions and is adjusted by changing the voltage applied across the DMA electrodes.[48] A condensation particle counter[49] (CPC, TSI Model 3776) was used to detect transmitted ions. The physical size of PEG_{4600}^{z+} ions is near the detection limit (minimum diameter) for the CPC, hence the ions were detected with imperfect efficiency using this approach, but the detection efficiency is likely not strongly charge state dependent.

Subsequent to PEG_{4600}^{z+} characterization we utilized the setup in Figure 2(b) to

examine ion-ion recombination induced charge reduction. Electrospray-generated PEG_{4600}^{z+} ions were mixed with not only negative, but positive ions (bipolar ions) generated in a separate chamber via the interaction of ^{241}Am-generated (~100 μCi) α-rays with UHP air. α-rays generate roughly equal concentrations of positive and negative ions, with recent work showing that these are largely derived from trace impurities, even in UHP air.[50-52] Generated negative ion concentrations in the mixing chamber (N_{ion}) were approximated via the method described in the supporting information with the set up depicted in Figure S2. Mobility distributions for ions were additionally measured with the DMA (connected to a Faraday cage electrometer, FCE),[53, 54] yielding a negative ion mean electrical mobility of 1.762 $cm^2\ V^{-1}\ s^{-1}$. While this mean value arises from a complex ion mixture and is not solely NO_2^- ions, it is in good agreement with previous measurements in UHP air,[50] and is used in subsequent comparison of calculations to measurements.

We explicitly studied recombination driven charge reduction for PEG ions using the experimental set up in Figure 1b. PEG_{4600}^{z+} ions were generated via an identical approach to that described for mass spectral characterization. The electrospray-generated ions were carried to a mixing chamber by UHP air with a volumetric flow rate of Q_{ES}. A second flow line brought in an ion laden flow from the ^{241}Am chamber, at a flow rate of Q_{Am}. Q_{ES} and Q_{Am} where varied such $Q_{\text{ES}}+Q_{\text{Am}}$ = 6.0 L min^{-1} for all test conditions. Within the mixing chamber, PEG_{4600}^{z+} and ^{241}Am-generated ions recombine, leading to shifts in the PEG_{4600}^{z+} charge state distribution to lower charge states. With a volume of 39.7 cm^3, the residence time in the mixing chamber was fixed at 0.397s, and the extent of charge reduction was dependent on the flow rate ratio, $Q_{\text{Am}}/Q_{\text{ES}}$. At the outlet of the mixing chamber, the mobility distributions of the PEG_{4600}^{z+} ions were measured using the DMA-CPC combination (with the CPC "blind" to smaller ^{241}Am ions because they are smaller than the critical size required for activation).[55] Using initial charge state distributions inferred from mass spectra

(supporting information Figure S3) and the set of differential equations described in the subsequent "*Results and Discussion Section*," we utilized dimensionless representations of the collision rate coefficient[56-58] along with experimentally inferred parameters to compare mobility distributions measured at variable Q_{Am}/Q_{ES} ratios to results. In this analysis, we assumed that the initial charge state distribution does not depend upon Q_{ES}.

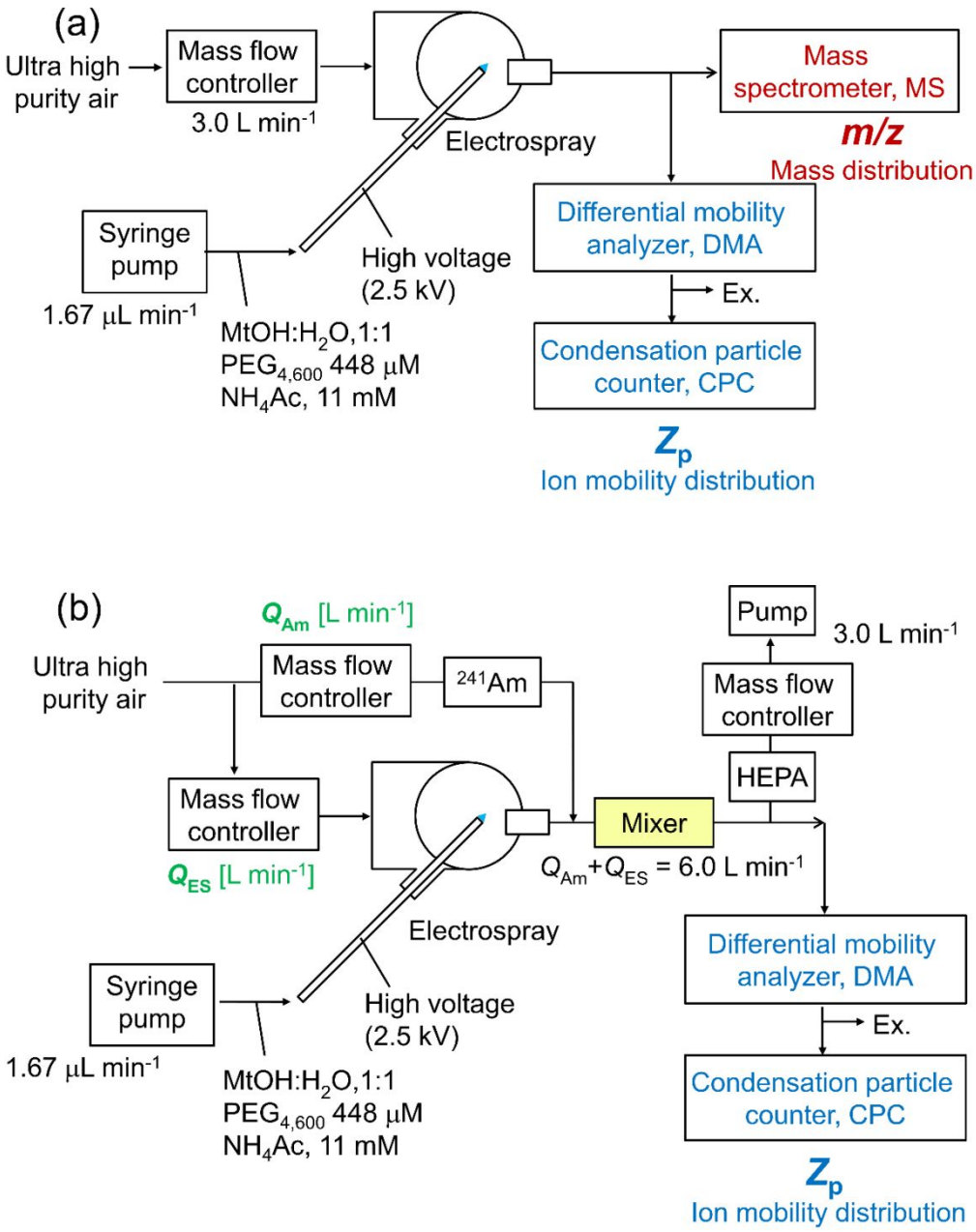

Figure 2. Schematic diagrams of the experimental setups used to measure initial properties (charge state distribution and mobility) of electrosprayed $PEG_{4,600}^{z+}$ ions **(a)** and to monitor the recombination-driven charge reduction process **(b)**. MFC: mass flow controller. Mixer:

Mixing chamber. HEPA: High efficiency particulate air filter.

Results& Discussion

Multiply Charged Ion Recombination Rate Coefficient

To our knowledge, the calculations presented here are the first effort to examine the ion-ion recombination driven charge reduction for multiply charged gas phase ions incorporating MD simulations into the calculation method towards the design of charge reduction systems for multiply charged polymer ions. As discussed in our initial presentation of continuum-MD simulation based recombination rate coefficient evaluation,[38] it is important to examine the influence of not only limiting sphere radius to ensure it is large enough, but also the collision distance. 5 Å was found to be sufficiently small in all instances and employed here; in prior work we show decreasing the collision radius below 4 Å does not affect results in comparison to 5 Å. While the maximum (upper limit) on collision distance which can be utilized does not directly influence results of either MD simulations or equation (1a) calculations, it remains important to determine, as it effectively is the "capture radius" for the collision under examination, and the capture radius is a necessary input to previously developed dimensionless recombination rate relationships. The inferred recombination rate coefficients from MD simulations and equations (1a-c) are plotted in Figure 3 as functions of the collision distance utilized. The same set of simulations is utilized to create results for each charge state; in all instances at least 100 collisions were ensured with 5 Å as the collision distance. As anticipated, beyond a critical collision distance, the inferred recombination rate begins to rise with increasing collision distance. To then quantify the critical collision distance, we define it as the distance at which the inferred recombination rate coefficient increases beyond 1.05x its value inferred at 5 Å. The critical collision distance from this definition increases with increasing charge state and with the exceptions of the $z = 1$ and $z = 2$ ions, the collision distance is substantially larger than physical sizes of

ions. Unsurprisingly, we can conclude that the critical distance for collision for highly charged ions is not governed by the physical sizes of ions, but is instead determined by the magnitude of the Coulombic potential energy in comparison to the thermal energy of the system; as this ratio rises above a critical value the ability of the ions to escape one another upon approach decreases substantially.[57, 59]

Guidelines, based upon the 5 Å collision distance results are also provided in Figure 3. The values for the z = 1 charge state, of 3.9 x 10^{-14} m^3 s^{-1} is lower than commonly reported for smaller ions in air or nitrogen,[29] however, as noted previously there is a lack of data on recombination rates for multiply charged ions, and for nanoscopic, multiply charged ions in general (comparison between theory and experiments in this size range is typically done more indirectly, e.g. via comparison to steady-state bipolar charge distributions[58, 60]). In line with the increase in critical collision distance, β_z is strongly dependent on the ion charge state, increasing by nearly three orders of magnitude as the charge state increases from $z = 1$ to $z = 7$. Table 1 summarizes the limiting sphere radius utilized, the collision distance estimated from Figure 3 plots, the inferred recombination rate coefficients from the smallest collision distance results, and the inferred radii of gyration from NVT simulations used to initialize PEG_{4600}^{z+} ions (±one standard deviation). Radii of gyration calculations confirm that in all circumstances, including $z = 1$ and $z = 2$ charge states, the collision distance inferred is larger than the PEG_{4600}^{z+} radius of gyration. Interestingly, the radius of gyration is nearly identical for the $z = 1$ and $z = 2$ charge states, which also have similar inferred collision distances, and is also similar for the $z = 4 - 6$ charge states, which also do not show a clear correlation between estimated collision distance and charge state. In Figure 4a we plot the estimate collision distance from Figure 3 as a function of charge state (purple circles), along with snapshots of NVT simulations of PEG_{4600}^{z+} ions. The $z = 1$ and $z = 2$ charge states gives rise to similar, unstretched ion structures. For z = 3 and larger charge

states, the PEG_{4600}^{z+} ions are progressively Coulombically stretched further and further, leading to a substantial increase in the radius of gyration by more than a factor of 5 as z spans from 1 to 7. The consistency of the radius of gyration and the collision distance in the $z = 4 - 6$ range is not necessarily expected. However, it is likely the result of the non-static ion structure; while ions elongate with increasing charge state, at intermediate charge states the polymer chain can bend and flex inward, evidenced by the large standard deviation in radius of gyration for the $z = 3 - 5$ charge states. Meanwhile, the collision distance is dependent on the potential, and is presumably not truly constant, but the estimation method utilized here (which does not affect the actual value of β_z) reported values are only approximations to the true value made in the absence of a rigorous definition.

Several recent efforts have been devoted to determining dimensionless rate coefficients applicable for particles and ions of variable sizes and shapes, as well as for a variety of potential interaction functional forms. Previous work along these lines has revealed that a dimensionless collision-controlled rate coefficient, $H(Kn_D,\Psi_E)$, can be defined accurately describing the collision rate coefficient across a wide temperature and pressure range, which is applicable for binary collisions of particles of arbitrary shape and vapor molecules,[61] ions,[57, 62] or other particles,[41, 63-65] and in the presence of short-range attractive[66] or short- and long-range repulsive interactions.[62] Such predictions have yielded good agreement with experimental measurements[58, 66, 67] and simulations[65, 68] in a variety of gas phase systems. In terms of the parameters relevant to multiply charged ion-ion recombination the dimensionless collision rate coefficient is expressed as:

$$H_{HS}(Kn_D) = \frac{\beta_z m_{red}\eta_c(D_z + D_-)}{k_b T L_C^3 \eta_f^2} = \frac{4\pi Kn_D^2 + 25.836 Kn_D^3 + \sqrt{8\pi}11.211 Kn_D^4}{1 + 3.502 Kn_D + 7.211 Kn_D^2 + 11.211 Kn_D^3} \quad (2a)$$

$$Kn_D = \sqrt{\frac{m_{red}}{k_b T}}\frac{(D_z + D_-)\eta_c}{L_C \eta_f} \quad (2b)$$

$$\eta_c = \frac{\Psi_E}{1 - exp(-\Psi_E)} \quad (2c)$$

$$\eta_f = 1 + \Psi_E \quad (2d)$$

$$\Psi_E = \frac{ze^2}{4\pi\varepsilon_0 k_b T L_C} \quad (2e)$$

where the subscript "HS" denotes that this equation originally arose from simulations of hard spheres,[41] with the enhancement factors η_c for the diffusive/continuum limit and η_f for the free molecular/ballistic limit added to account for the influence of potentials in later studies.[57] In equation (2b), Kn_D is the diffusive Knudsen number,[69] which is proportional to ratio of the fully diffusive collision rate coefficient to the free molecular rate coefficient. In equations (2a), (2b), and (2e), L_C is the collision length; in prior work this has been treated as the sum of the radii of colliding spheres[66] or defined in terms of clear structural descriptors for rigid non-spherical structures.[61] However, as noted in our prior study,[38] and elsewhere[57] for ion-ion recombination this distance needs to be defined based not on the physical sizes but a critical collision distance akin to that examined in Figure 4a. Therefore, while we again note that the determined collision distances are approximate, their implementation offers the opportunity to compare equation (2a) predictions to simulations. Using the table 1 collision distances, we arrive at $\Psi_E = 33.5, 90.5, 30.6, 22.2, 37.5, 33.4$ and 15.83, and $Kn_D = 32.3, 44.3, 9.71, 5.27, 7.23, 5.34$ and 2.10, respectively, as z increases from 1 to 7. Comparison between equation (2a) and continuum-MD calculations using these values is provided in Figure 4b. Equation (2a), by construction, correctly converges to the dimensionless collision rate in the low pressure[70] and high pressure limits[40] for all attractive and repulsive Coulomb potential magnitudes. Nonetheless, we anticipate that equation (2a) predictions should be smaller than continuum-MD predictions; Gopalakrishnan & Hogan[57] found that uniquely, in the presence of strong Coulombic attractive interactions (high Ψ_E) and elevated diffusive Knudsen number (high Kn_D), neither the low pressure nor high pressure limiting expressions are necessarily accurate, and equation (2a) will underestimate the true dimensionless collision rate coefficient. With the exception of the $z = 1$, charge state, we

find this conclusion remains valid here, and the "hard-sphere" dimensionless collision rate coefficients are a factor of 2-5 lower than the continuum-MD-inferred coefficients. To further compare calculations to prior results, similarly plotted in Figure 4b is the adjusted curve of Chahl & Gopalakrishnan,[56] designed to correct equation (2a) for high Ψ_E and high Kn_D conditions:

$$H(Kn_D,\Psi_E) = \frac{\beta_z m_{red}\eta_c(D_{z+} + D_-)}{k_b T L_C^3 \eta_f^2} = e^{\mu(Kn_D,\Psi_E)} H_{HS}(Kn_D) \quad (3a)$$

$$\mu(Kn_D,\Psi_E) = \frac{C}{A}\left(1 + k\frac{ln(Kn_D) - B}{A}\right)^{-\frac{1}{k}-1} exp\left[-\left(1 + k\frac{ln(Kn_D) - B}{A}\right)^{-\frac{1}{k}}\right] \quad (3b)$$

$$A = 2.5 \quad (3c)$$

$$B = 4.528exp(-1.088\Psi_E) + 0.7091ln(1 + 1.537\Psi_E) \quad (3d)$$

$$C = 11.36\Psi_E^{0.272} - 10.33 \quad (3e)$$

$$k = -0.003533\Psi_E + 0.05971 \quad (3f)$$

$H_{HS}(Kn_D)$ is equation (3a) denotes the equation (2a) definition in terms of diffusive Knudsen number. The Chahl & Gopalakrishnan[56] expression has been shown yield results in good agreement with unipolar and bipolar aerosol particle ionization measurements with particles > 2 nm in diameter.[58, 71] It also agrees well with expressions developed by Gatti & Kortshagen[72] for positive ion-negatively charged particle collisions in a plasma near $\Psi_E = 30$, hence the comparison we provide here can be extrapolated to other theories. Equation (3a) predictions appear to overcorrect the hard-sphere curve, leading to a larger dimensionless collision rate coefficient than continuum-MD calculations. However, while in equation (2a), L_C in the presence of strong attractive Coulomb interactions is defined as a capture radius,[57] in equation (3a) the physical sizes of the ions should be used to define L_C.[58] For this reason, we also attempted to fit values of L_C to force agreement between $H(Kn_D,\Psi_E)$ from continuum-MD simulations and equation (3a). In this effort we found that the

functional form of equation (3a) does not permit exact agreement with any input L_C. We conclude that more work is needed to rectify differences in recombination rates from continuum-MD predictions for multiply charged, flexible ions, and dimensionless approaches based on Langevin dynamics simulations for rigid aerosol particles; in particular additional work is needed to determine a proper manner of defining L_C for an apt comparison.

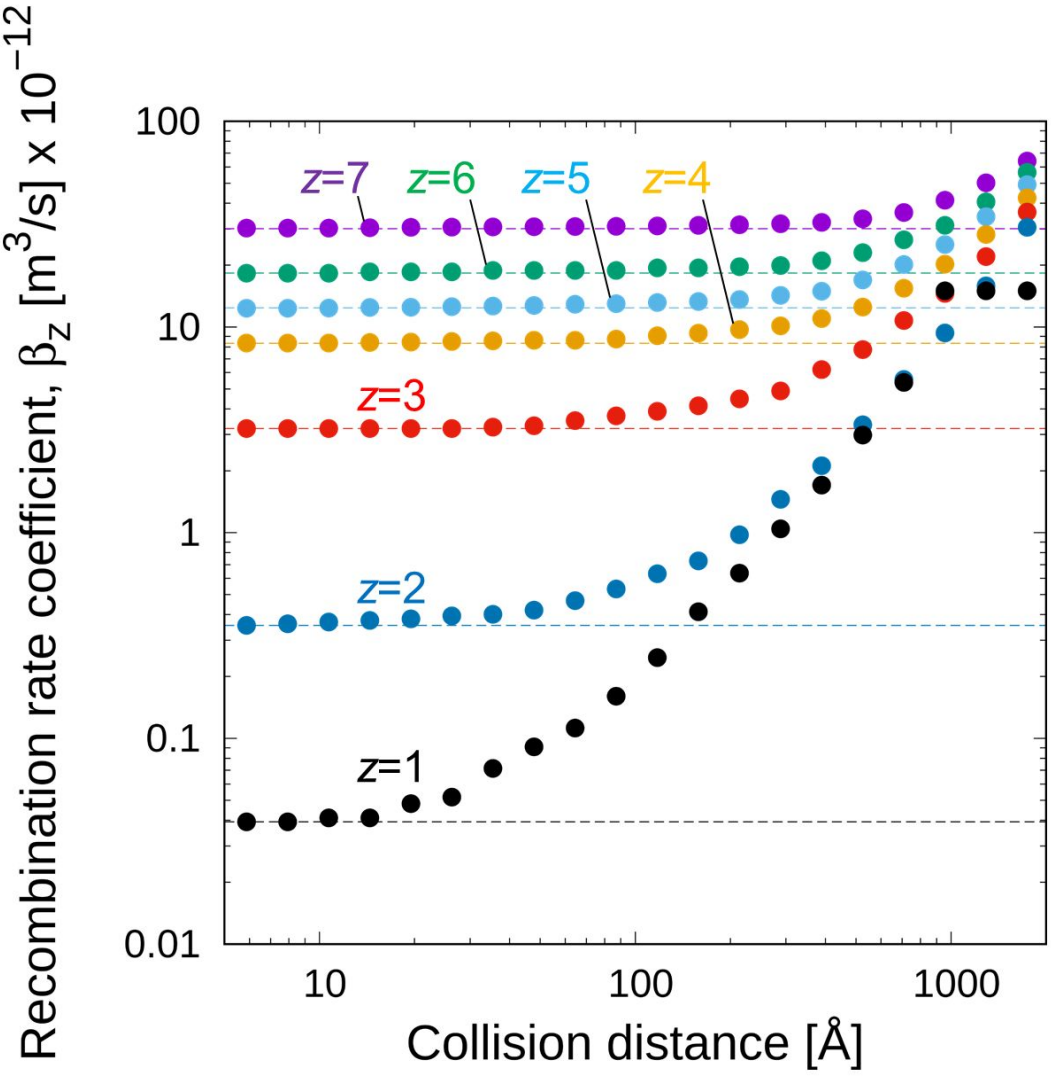

Figure 3. The recombination rate coefficient β_z inferred from continuum-MD simulations as a function of the collision distance used in simulations to identify collisions.

Table 1. A summary of the limiting sphere radius, inferred collision distance, inferred recombination rate coefficient, and calculated radii of gyration for different charge states of PEG_{4600}^{z+}.

Charge state	Limiting sphere radius, δ [Å]	Collision distance [Å]	Recombination rate coefficient, β_z [m^3/s] x 10^{-12}	Radius of Gyration, R_g [Å]
z=1	1056.6	16.57	0.0393	10.4 ± 0.1
z=2	1761.0	12.28	0.354	10.4 ± 0.1
z=3	1761.0	54.93	3.21	39.3 ± 17.4
z=4	1761.0	100.00	8.34	45.0 ± 16.6
z=5	1761.0	74.11	12.3	45.5 ± 12.4
z=6	1761.0	100.00	18.3	45.8 ± 3.4
z=7	1761.0	245.65	30.2	55.2 ± 6.2

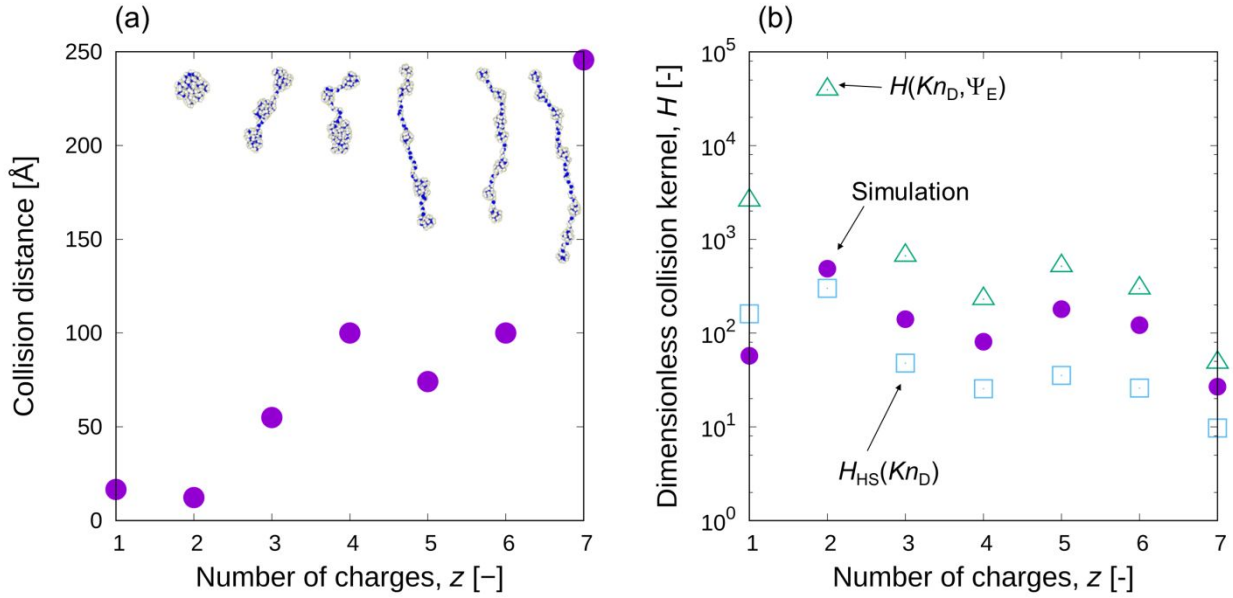

Figure 4. The estimated collision distance as a function of the net number of charges (charge state) on the PEG_{4600}^{z+} ion **(a)**; a comparison of continuum-MD simulation results expressed as a dimensionless recombination rate coefficient (equation 2a) in comparison to previously developed dimensionless collision rate expressions (equation 3, $H_{HS}(Kn_D)$ and equation 4a $H(Kn_D,\Psi_E)$) **(b)**.

Charge Reduction Rate

Comparison of measurements to theoretical predictions of charge reduction is

complicated by the need to determine the initial charge state distribution of PEG_{4600}^{z+} ions, and adapt theory for the true mobilities of ions utilized, which differs from the mobility of NO_2^- ions used in calculations. Also noteworthy are that the recombination rate coefficient appears to vary by orders of magnitude with change in charge state, the charge reduction rate is sensitive to linear charges in the recombination rate coefficient, and there are experimental uncertainties associated with charge state distribution inference from mobility measurements. We thus approach comparison such that we view agreement of the charge state distribution evolution with models bounded by $0.5\beta_{z,\mathrm{sim}} \leq \beta_z \leq 2.0\beta_{z,\mathrm{sim}}$, where "sim" denotes continuum-MD results, as support for the use of continuum-MD calculations.

Experimental-theoretical comparison ultimately hinges on comparison of the measured fraction of ions f_z in a population of charge state of charge state z, after exposure to negative ions of known concentration N_{ion} and known exposure time t. In experiments, the residence time is fixed via the mixer geometry and use of constant system volumetric flow rates, while ion concentration is controlled via varying the flow rate ratio ($Q_{\mathrm{Am}}/Q_{\mathrm{ES}}$). Theoretically, f_z evolves via recombination induced charge reduction by the equations:

$$\frac{df_z}{dt} = \left(\frac{k_b T N_{\mathrm{ion}}}{m_{\mathrm{red}}(D_z + D_-)}\right)\left(\frac{L_{C,z+1}^3 \eta_{f,z+1}{}^2 H_{z+1}}{\eta_{c,z+1}} f_{z+1} - \frac{L_{C,z}^3 \eta_{f,z}{}^2 H_z}{\eta_{c,z}} f_z\right) \quad (4)$$

where the subscripts z and $z+1$ denote parameters for the charge state in question and one unit charge level higher, respectively, and N_{ion} is the negative ion concentration. In equation (4), the reduced mass and diffusion coefficient of the multiply charged ion are assumed independent of z; the latter assumption is only reasonable because $D_z \ll D_-$.

To compare equation (4) to experiments requires solution to the set equations given by equation (4), which requires initial conditions for f_z matching experiments. In Figure 5a we plot the initial electrical mobility distribution of PEG_{4600}^{z+} ions measured via the DMA-CPC combination. Two peaks are present in these spectra. Prior experience[73] in examining

the electrical mobility spectra of multiply charged, stretched macromolecular ions with mass spectrometry informs us that the lower electrical mobility peak corresponds to aggregates ($(PEG_{4600})_n^{z+}$, which are less stretched as they can accommodate higher charge levels and remain globular,[32, 34, 36] and the higher electrical mobility peak is stretched, monomeric ions. The aggregates are typically formed non-specifically[74] at the PEG_{4600} concentrations employed in the experiments here; at the same time such high concentrations are required for appreciable monomer signal in DMA-CPC measurements. For the monomer peak, the mobilities of stretched ions are largely independent of charge state, i.e. the ion collision cross section is approximately proportional to the charge state z in the regime where Coulombic stretching occurs.[35, 38] Therefore, electrical mobility spectra alone cannot provide proper initial charge state distributions for the ions. Conversely, mass spectrometric measurements with an upper m/z limit of 2000 Th are largely shielded from aggregate peaks (above 2000 Th), and with fitting, can provide an estimate of f_z. This two-step fitting procedure, utilizing the electrical mobility of the $z = 1$ charge state to determine a true mean molecular weight for the PEG_{4600}^{z+} ions and then fitting to the mass spectrum, is described in the supporting information, including Figures S3 (mass spectrum) and S4 (mobility spectrum). Fitting results lead to non-zero initial values for f_z in the $3 \leq z \leq 7$ range, which are used in initial conditions. Measurement of the singly charged PEG ions additionally serves to evaluate the diffusion coefficient of the PEG_{4600}^{z+} ions, input into calculations (equation 1a). The electrical mobility value measured here of Z_p = 0.28 $cm^2\ V^{-1}\ s^{-1}$ is in excellent agreement with 0.27 $cm^2\ V^{-1}\ s^{-1}$ from Saucy et al.[4]

Figure 5b displays plots of the relative electrical mobility spectra obtained with variable bipolar ion source to electrospray source flow rate ratio (Q_{Am}/Q_{ES}). As Q_{Am}/Q_{ES} increases, increasing N_{ion} (as described in the supporting information) leads to new, reasonably narrow peaks in the electrical mobility spectra. We attribute the lowest electrical

mobility peak near 0.28 $cm^2\ V^{-1}\ s^{-1}$, which emerges at the higher values of Q_{Am}/Q_{ES}, to the $z = 1$ ion, as this is near the expected electrical mobility for singly charged PEG ions of mass 4339 Da.[4] An intermediate peak, at nearly double the electrical mobility, we attribute to $z = 2$ ions, and the original, highest electrical mobility peak, we attribute to $z = 3 - 7$ ions (of similar mobility due to stretching). In conjunction with the appearance of the new peaks, the peak originally attributed to aggregates broadens appreciably as Q_{Am}/Q_{ES} increases and its range shifts to ever smaller electrical mobilities, confirming this peak is attributable to aggregate ions. Red "fit" curves are used to denote the monomer peaks in Figure 4b, while black is utilized for the aggregate peak. Fitting was carried out using four normal distributions (one of the each of the $z = 1$, $z = 2$, $z = 3 - 7$, and aggregate peaks). We remark that results are not corrected for electrostatic losses, which can be significant for multiply charged ions.[75] In total, peak intensities in the electrical mobility spectra in Figure 5b provide values for f_1, f_2, and f_{3-7}. Combined with the initial conditions from mass spectrometer fitting, we are able to compare equation (4) predictions to experiments. In comparison, the values of H_z in equation (4) are taken directly from continuum-MD calculations without adjustment, equation (2a), and equation (3a); for the latter two we use L_C values directly from Table 1. The diffusion coefficient of the anions D_- is adjusted to match values inferred from experimental mobility measurements. The resulting comparison between predictions and measurements is provided in figure 6, which specifically displays plots of f_1, f_2, and f_{3-7} as functions of ion concentration. Lines for continuum-MD simulation predictions (long dash lines) as well as those corresponding to a shift in all H_z values by 0.5 or 2.0 (short dash lines) are displayed in each plot, along with equation (2a) and equation (3a) predictions (solid lines). In all conditions except for several f_1 points, the experimentally inferred values are indeed bounded by the $0.5\beta_{z,sim} \leq \beta_z \leq 2.0\beta_{z,sim}$ (shaded region). By comparison to equation (2a) and (3a) predictions, it is also apparent that f_z

evolution is strongly sensitive to the recombination rate coefficient, and the modest agreement observed between experiments and continuum-MD simulations is strong support for the validity of the continuum-MD approach in recombination rate calculation.

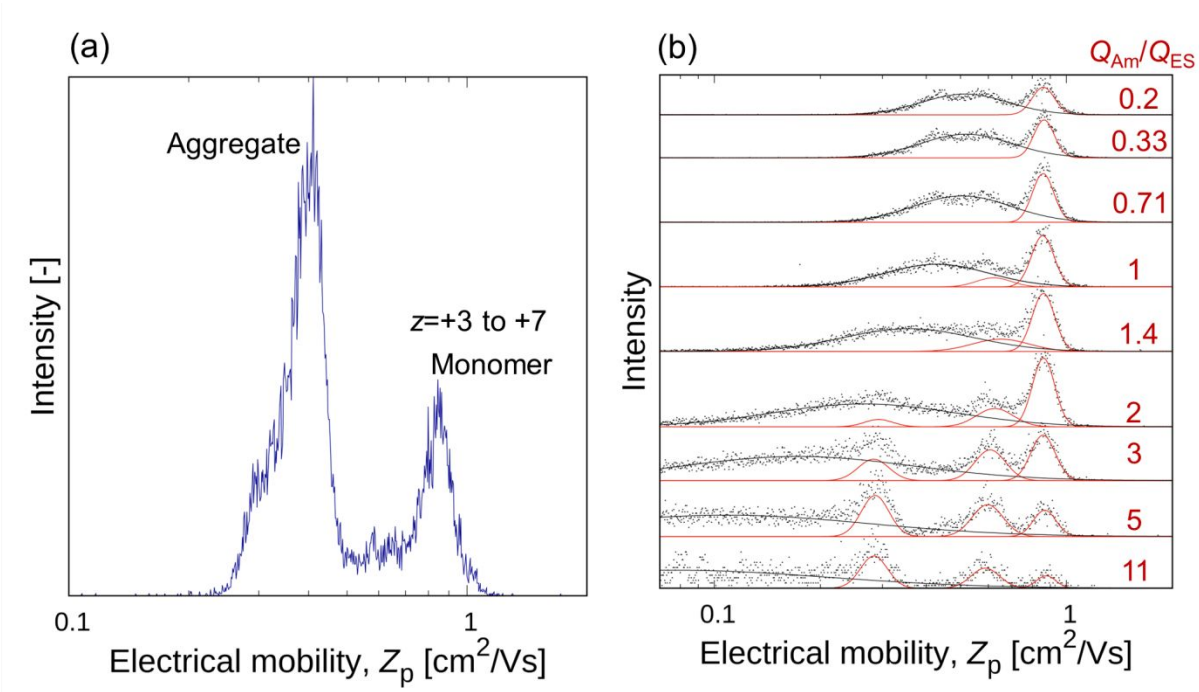

Figure 5. The electrical mobility distributions of PEG_{4600}^{z+} ions as electrosprayed **(a)** and as a function of the bipolar ion source to electrospray source flow rate ratio **(b).**

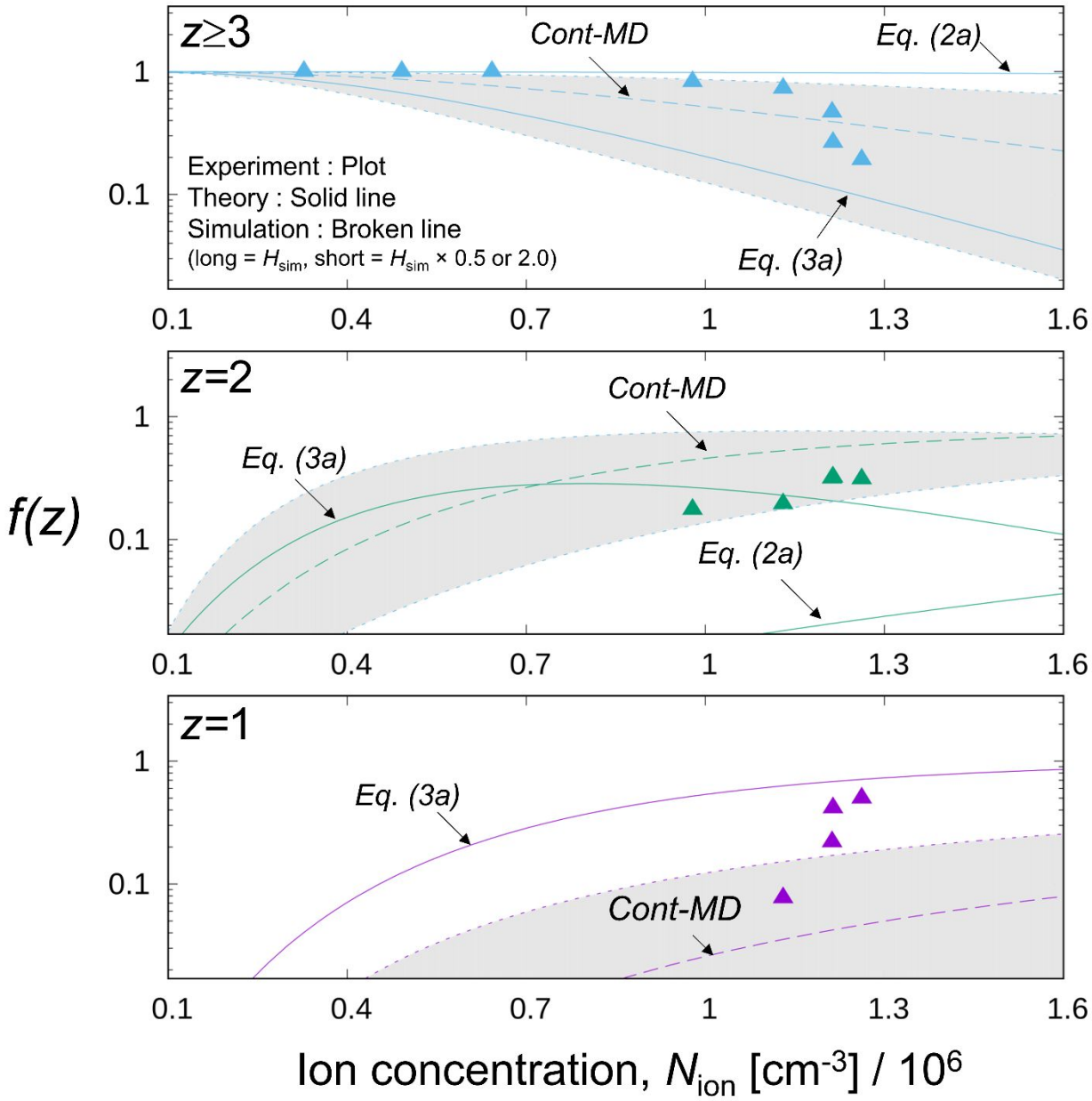

Figure 6. Charge fractions inferred from electrical mobility spectra in comparison to equation (5) predictions using equations (3), (4), and continuum-MD (cont-MD) simulation predictions. The short dashed lines denote application of equation (5) with $H_z = 0.5H_{z,\mathrm{sim}}$ and $H_z = 2.0H_{z,\mathrm{sim}}$, where $H_{z,\mathrm{sim}}$ results from non-dimensionalization of continuum-MD simulations.

Collisional Energy

A final parameter of interest for Coulombically driven collisions between the low and high pressure limits is the translational velocity and corresponding kinetic energy at collision. Using the 5 Å collision distance we estimate the probability density function on the collision

velocity in Figure 7. The mean thermal speed of an NO_2^- ion at 300 K is 371 m s^{-1}. Collisional velocities increase with increasing charge state, and mean values are nearly and order of magnitude higher than the mean thermal velocity. For $z = 7$, the mean translational kinetic energy at collision is ~2.2 eV. Using the specific heat of ethylene glycol (2433 J kg^{-1} K^{-1}), assuming full accommodation and equilibration of this energy a 4600 Da ion, each ion collision would elevate the "temperature" of the PEG_{4600}^{z+} ion by 18.9 K for $z = 7$. This is likely too small to catalyze any reaction within PEG_{4600}^{z+} ion unless energy is partitioned non-ergodically during collision. However, smaller ions would less able to accommodate an energy increase of order 1 eV, and in certain circumstances, ion-ion recombination, even at atmospheric pressure, may drive collision induced dissociation or other chemical reactions which would not be observed during the collision of an ion and neutral species.

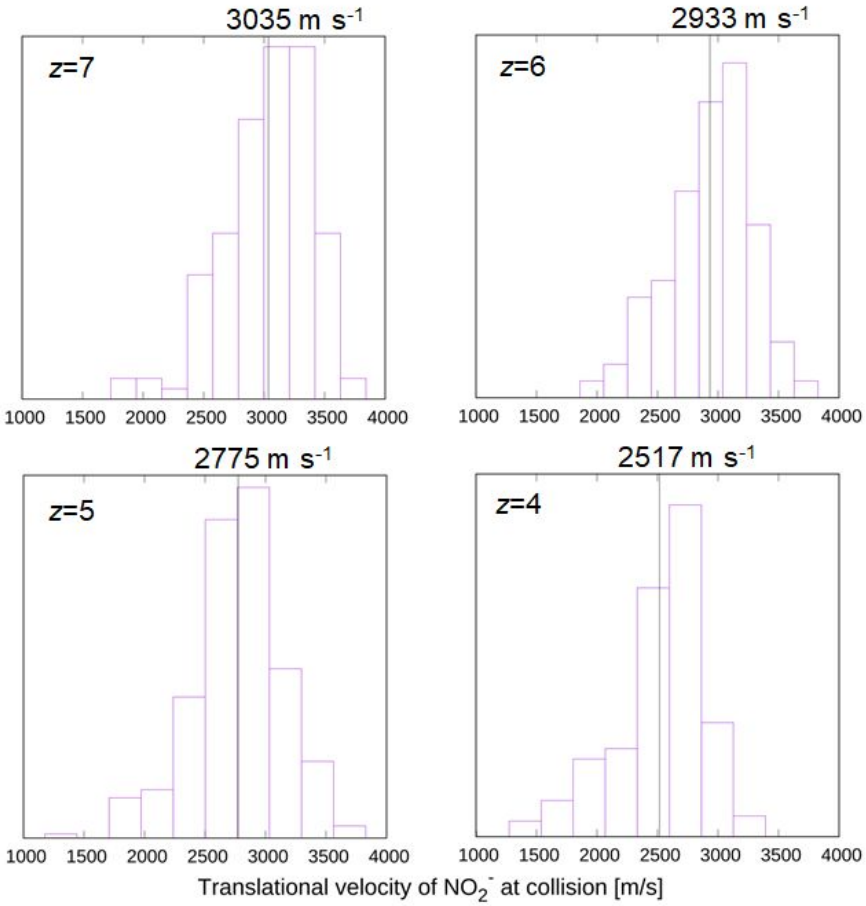

Figure 7. Probability density functions (binned, relative values) for the NO_2^- velocity at collision. The mean value is noted for each charge state.

Conclusions

We utilize a combination of continuum-MD simulations and electrical mobility based measurements to examine recombination-induced charge reduction in PEG_{4600}^{z+} ions. In terms of collision-induced reactions in the gas phase, recombination-induced charge reduction of polymer ions at atmospheric pressure is extremely unique because it can be described by neither low pressure nor high pressure recombination rate theories, the Coulomb energy vastly exceeds thermal energy in magnitude, and the polymer ion is flexible, adopting charge state-specific conformational distributions. All of these features are accounted for in continuum-MD simulations, and despite several noted ambiguities in interpretation of experiments, we find good agreement between numerical models of charge reduction based upon continuum-MD simulations, and the evolution the charge state distribution of PEG_{4600}^{z+} ions inferred from atmospheric pressure electrical mobility measurements. Beyond this broad conclusion, we also note that comparison to Langevin dynamics based expressions[56, 57] for the dimensionless recombination rate coefficient shows that while such theories appear successful for rigid ions and particles of fixed structure, for flexible ions with highly attractive Coulombic potentials, the collision distance, needed as an input in utilizing such expressions, is not yet clarified. The continuum-MD calculation approach yields directly the recombination rate coefficient without needing an input collision distance. Nonetheless the collision distance remains of interest in developing a universal theory for collision rate coefficients in the gas phase, bridging particle-particle collisions to ion-ion recombination.

We also conclude by remarking on the future potential of the continuum-MD approach in examining the dynamics of highly charged ions in atmospheric pressure systems or higher pressure systems. Through the use of sub-domains, the number of neutral gas molecules needed to accurately model ion dynamics can be made insensitive to pressure, enabling application to examine a wide variety of systems. Examination of even larger

biomolecular systems, the inclusion of adsorbed water molecules, and three-body interactions are all possible with this approach (though the latter would require modification of the continuum equations invoked). Overall, we suggest continuum-MD simulations are a general approach to examine collision driven reactions across a wide pressure range, incorporating precisely the conformational dynamics of reacting species.

Supporting Information

A supplemental .pdf file contains information on the selection of the limiting sphere radius, a table denoting partial charges on PEG_{4600}^{z+} atoms, notes on application of the ion-induced dipole potential, a description of singly charged ion concentration measurements, a plot of the mass spectrum of PEG_{4600}^{z+} prior to charge reduction, a note on fitting of the mobility distribution for singly PEG ions, and evaluation of the initial PEG_{4600}^{z+} charge distribution. Supplemental videos depicting trajectories of ions and their domains from selected simulations with $z = 7$ are also available online. Videos were made with Ovito.

Conflicts of interest

There are no conflicts to declare.

Acknowledgements.

Computations were performed using computing resources at the Research Center for Computational Science, Okazaki, Japan. T. T. and T. S. were supported by the Hosokawa Powder Technology Foundation (T. T. was for the young researcher award). H. H. and T. S. were supported by JST CREST Grant Number JPMJCR18H4, Japan. C.J.H. acknowledges support from Department of Energy Award No. DE-SC0018202.

References

1. S. J. Pitteri and S. A. McLuckey, *Mass Spectrometry Reviews*, 2005, **24**, 931-958.
2. S. A. McLuckey and T.-Y. Huang, *Analytical Chemistry*, 2009, **81**, 8669-8676.
3. B. K. Ku, J. Fernandez de la Mora, D. A. Saucy and Alexander, *Analytical Chemistry*, 2004, **76**, 814-822.
4. D. A. Saucy, S. Ude, I. W. Lenggoro and J. Fernandez de la Mora, *Analytical Chemistry*, 2004, **76**, 1045-1053.
5. C. S. Kaddis, S. H. Lomeli, S. Yin, B. Berhane, M. I. Apostol, V. A. Kickhoefer, L. H. Rome and J. A. Loo, *Journal of the American Society for Mass Spectrometry*, 2007, **18**, 1206-1216.
6. S. L. Kaufman, J. W. Skogen, F. D. Dorman, F. Zarrin and K. C. Lewis, *Analytical Chemistry*, 1996, **68**, 1895-1904.
7. G. Bacher, W. W. Szymanski, S. L. Kaufman, P. Zöllner, D. Blaas and G. Allmaier, *Journal of Mass Spectrometry*, 2001, **36**, 1038-1052.
8. J. L. Stephenson and S. A. McLuckey, *Journal of the American Chemical Society*, 1996, **118**, 7390-7397.
9. S. Mouradian, J. W. Skogen, F. D. Dorman, F. Zarrin, S. L. Kaufman and L. M. Smith, *Analytical Chemistry*, 1997, **69**, 919-925.
10. D. D. Ebeling, M. S. Westphall, M. Scalf and L. M. Smith, *Analytical Chemistry*, 2000, **72**, 5158-5161.
11. M. Scalf, M. S. Westphall, J. Krause, S. L. Kaufman and L. M. Smith, *Science*, 1999, **283**, 194.
12. R. R. Abzalimov and I. A. Kaltashov, *Analytical Chemistry*, 2010, **82**, 7523-7526.
13. C. J. Hogan, R. R. Ogorzalek Loo, J. A. Loo and J. Fernandez de la Mora, *Physical Chemistry Chemical Physics*, 2010, **12**, 13476-13483.
14. J. Fernandez de la Mora, *Analytical Chemistry*, 2015, **87**, 3729-3735.
15. J. V. Iribarne and B. A. Thomson, *The Journal of Chemical Physics*, 1976, **64**, 2287-2294.
16. M. Gamero-Castaño and J. F. d. l. Mora, *Journal of Mass Spectrometry*, 2000, **35**, 790-803.
17. M. Hautreux, N. Hue, A. Du Fou de Kerdaniel, A. Zahir, V. Malec and O. Laprévote, *International Journal of Mass Spectrometry*, 2004, **231**, 131-137.
18. I. A. Kaltashov and A. Mohimen, *Analytical Chemistry*, 2005, **77**, 5370-5379.
19. J. Fernandez de la Mora, *Analytica Chimica Acta*, 2000, **406**, 93-104.
20. C. J. Hogan, J. A. Carroll, H. W. Rohrs, P. Biswas and M. L. Gross, *Analytical Chemistry*, 2009, **81**, 369-377.
21. W. Peukert and C. Lübbert, *The Journal of Physical Chemistry A*, 2020, **10.1021/acs.jpca.0c05076**, In Press.
22. L. B. Loeb, *Physical Review*, 1937, **51**, 1110-1111.
23. L. B. Loeb and L. C. Marshall, *Journal of the Franklin Institute*, 1929, **208**, 371-388.
24. J. J. Thomson, *The London, Edinburgh, and Dublin Philosophical Magazine and Journal of Science*, 1924, **47**, 337-378.
25. P. Langevin, *Annales de chimie et de physique*, 1903, **28**, 433-530.
26. G. Natanson, *Soviet Physics Technical Physics*, 1960, **5**, 538-551.
27. K. A. Brueckner, *The Journal of Chemical Physics*, 1964, **40**, 439-444.
28. D. R. Bates and M. R. Flannery, *Journal of Physics B: Atomic and Molecular Physics*, 1969, **2**, 184-190.
29. A. Franchin, S. Ehrhart, J. Leppä, T. Nieminen, S. Gagné, S. Schobesberger, D. Wimmer, J. Duplissy, F. Riccobono, E. M. Dunne, L. Rondo, A. Downard, F.

Bianchi, A. Kupc, G. Tsagkogeorgas, K. Lehtipalo, H. E. Manninen, J. Almeida, A. Amorim, P. E. Wagner, A. Hansel, J. Kirkby, A. Kürten, N. M. Donahue, V. Makhmutov, S. Mathot, A. Metzger, T. Petäjä, R. Schnitzhofer, M. Sipilä, Y. Stozhkov, A. Tomé, V. M. Kerminen, K. Carslaw, J. Curtius, U. Baltensperger and M. Kulmala, *Atmos. Chem. Phys.*, 2015, **15**, 7203-7216.
30. H. S. Lee and R. Johnsen, *The Journal of Chemical Physics*, 1989, **90**, 6328-6334.
31. D. R. Bates, *Planetary and Space Science*, 1982, **30**, 1275-1282.
32. S. Ude, J. Fernández de la Mora and B. A. Thomson, *Journal of the American Chemical Society*, 2004, **126**, 12184-12190.
33. E. Criado-Hidalgo, J. Fernández-García and J. Fernández de la Mora, *Analytical Chemistry*, 2013, **85**, 2710-2716.
34. C. Larriba and J. Fernandez de la Mora, *The Journal of Physical Chemistry B*, 2012, **116**, 593-598.
35. X. Chen, S. A. Raab, T. Poe, D. E. Clemmer and C. Larriba-Andaluz, *Journal of the American Society for Mass Spectrometry*, 2019, **30**, 905-918.
36. C. Larriba, J. Fernandez de la Mora and D. E. Clemmer, *Journal of the American Society for Mass Spectrometry*, 2014, **25**, 1332-1345.
37. D. Morsa, T. Defize, D. Dehareng, C. Jérôme and E. De Pauw, *Analytical Chemistry*, 2014, **86**, 9693-9700.
38. T. Tamadate, H. Higashi, T. Seto and C. J. Hogan, *The Journal of Chemical Physics*, 2020, **152**, 094306.
39. A. V. Filippov, *J Aerosol Sci*, 1993, **24**, 423-436.
40. N. A. Fuchs, *Geofis. Pura Appl.*, 1963, **51**, 185-193.
41. R. Gopalakrishnan and C. J. Hogan, *Aerosol Science and Technology*, 2011, **45**, 1499-1509.
42. H. Tammet, *J Aerosol Sci*, 1995, **26**, 459-475.
43. P. G. Wright, *Discussions of the Faraday Society*, 1960, **30**, 100-112.
44. S. Plimpton, *Journal of Computational Physics*, 1995, **117**, 1-19.
45. J. Wang, R. M. Wolf, J. W. Caldwell, P. A. Kollman and D. A. Case, *Journal of Computational Chemistry*, 2004, **25**, 1157-1174.
46. T. Tamadate, T. Orii, H. Higashi, Y. Otani, M. Kumita and T. Seto, *Aerosol Science and Technology*, 2019, **53**, 260-267.
47. J. Fernandez de la Mora, L. de Juan, T. Eichler and J. Rosell, *Trac-Trend Anal Chem*, 1998, **17**, 328-339.
48. M. R. Stolzenburg and P. H. McMurry, *Aerosol Science and Technology*, 2008, **42**, 421-432.
49. M. R. Stolzenburg and P. H. Mcmurry, *Aerosol Science and Technology*, 1991, **14**, 48-65.
50. A. Maißer, J. M. Thomas, C. Larriba-Andaluz, S. He and C. J. Hogan Jr, *J Aerosol Sci*, 2015, **90**, 36-50.
51. G. Steiner and G. P. Reischl, *J Aerosol Sci*, 2012, **54**, 21-31.
52. Y. Liu, M. Attoui, K. Yang, J. Chen, Q. Li and L. Wang, *J Aerosol Sci*, 2020, **147**, 105586.
53. X. Chen, T. Seto, U. R. Kortshagen and C. J. Hogan, *Nano Futures*, 2019, **3**, 015002.
54. G. P. Reischl, J. M. Mäkelä and J. Necid, *Aerosol Science and Technology*, 1997, **27**, 651-672.
55. J. Kangasluoma and M. Attoui, *Aerosol Science and Technology*, 2019, **53**, 1277-1310.
56. H. S. Chahl and R. Gopalakrishnan, *Aerosol Science and Technology*, 2019, **53**, 933-957.

57. R. Gopalakrishnan and C. J. Hogan, *Physical Review E*, 2012, **85**, 026410.
58. L. Li, H. S. Chahl and R. Gopalakrishnan, *J Aerosol Sci*, 2020, **140**, 105481.
59. S. A. Khrapak, S. V. Ratynskaia, A. V. Zobnin, A. D. Usachev, V. V. Yaroshenko, M. H. Thoma, M. Kretschmer, H. Höfner, G. E. Morfill, O. F. Petrov and V. E. Fortov, *Physical Review E*, 2005, **72**, 016406.
60. T. J. Johnson, R. T. Nishida, M. Irwin, J. P. R. Symonds, J. S. Olfert and A. M. Boies, *J Aerosol Sci*, 2020, **143**, 105526.
61. R. Gopalakrishnan, T. Thajudeen and C. J. Hogan, *Journal of Chemical Physics*, 2011, **135**, 054302.
62. R. Gopalakrishnan, T. Thajudeen, H. Ouyang and C. J. Hogan, *J Aerosol Sci*, 2013, **64**, 60-80.
63. A. M. Boies, C. Hoecker, A. Bhalerao, N. Kateris, J. de La Verpilliere, B. Graves and F. Smail, *Small*, 2019, **15**, 1900520.
64. T. Thajudeen, R. Gopalakrishnan and C. J. Hogan, *Aerosol Science and Technology*, 2012, **46**, 1174-1186.
65. J. Morán, J. Yon, A. Poux, F. Corbin, F. X. Ouf and A. Siméon, *Journal of Colloid and Interface Science*, 2020, **575**, 274-285.
66. H. Ouyang, R. Gopalakrishnan and C. J. Hogan, *The Journal of Chemical Physics*, 2012, **137**, 064316.
67. M. Yu, J. Lin, M. Seipenbusch and J. Cao, *Chemical Engineering Journal*, 2017, **323**, 592-604.
68. E. Goudeli, M. L. Eggersdorfer and S. E. Pratsinis, *Langmuir*, 2015, **31**, 1320-1327.
69. B. E. Dahneke, in *Theory of Dispersed Multiphase Flow*, ed. R. E. Meyer, Academic Press, New York1983.
70. J. E. Allen, *Phys. Scr.*, 1992, **45**, 497-503.
71. L. Li and R. Gopalakrishnan, *J Aerosol Sci*, 2020, 105678.
72. M. Gatti and U. Kortshagen, *Physical Review E*, 2008, **78**, 046402.
73. C. J. Hogan and J. Fernandez de la Mora, *Journal of the American Society for Mass Spectrometry*, 2011, **22**, 158-172.
74. K. L. Davidson, D. R. Oberreit, C. J. Hogan and M. F. Bush, *International Journal of Mass Spectrometry*, 2017, **420**, 35-42.
75. M. Attoui and J. F. de la Mora, *J Aerosol Sci*, 2016, **100**, 91-96.

The charge reduction (recombination) rate of highly charged polyethylene glycol ions was estimated by Continuum-Molecular dynamics simulation and compered with experimental IMS measurements.